Nanoplasmonic hybrid hotspot in graphene transistor

Fatemeh Safarzadeh and Mahmood Hosseini Farzad*
Physics Department, College of Sciences, Shiraz University, Shiraz 71454, Iran

(Received 13 October 2022; revised 22 January 2023; accepted 24 January 2023; published 27 February 2023)

A field effect transistor based on graphene was introduced to generate a hybrid plasmonic mode. The main reasons to consider graphene in this study are the achievement of high field confinement and the graphene two carrier transport channel near its charge neutrality point. We have observed a nonlinear behavior of the hybrid plasmonic mode near the graphene charge neutrality point because of the existence of the two carrier model. This nonlinear behavior reflects the intrinsic nanoelectronic characteristics of graphene. The proposed nanoelectronic device presents an ultraconfined tunable hybrid hotspot, the mode area of which is 10^5 times smaller than the diffraction limited spot area. Moreover, this area is three orders of magnitude smaller than the modal area of the similar metal-based hybrid nanostructure. Such a nanoscale 3D hotspot with plasmonic-photonic character has been reported here. Furthermore, a hybrid structure based on bilayer twisted graphene was numerically investigated which renders ultrahigh confinement and ultralong propagation distance. The proposed nanodevice can be applied to design compact integrated circuits, optical neural networks, and high resolution sensors.

DOI: 10.1103/PhysRevB.107.075439

I. INTRODUCTION

Photonics has been investigated tremendously as one of the physical sciences in the field of light waves [1–3]. However, one of the serious obstacles faced by various photonic studies was diffraction limit, constraining researchers in manipulation of light at will [4]. Plasmonics was fast becoming a key instrument in this topic. Plasmonics is an optical phenomenon created by coupling of electromagnetic waves with free electrons at a metal-dielectric interface. This coupling forces the light to experience high confinement near the interface, resulting in considerable field enhancement in a deep subwavelength area [5–8]. Tuning of light in subwavelength scales is a research hotspot because of its prominent role in nanoscience and nanotechnology. These capabilities of plasmonic modes hold promise for potential applications in nonlinear optics [9–13], biochemical sensors [14–16], nanoimaging [17–20], magneto-optic data storage [21], and solar cells [7,22].

One of the promising applications of plasmonic modes is their contribution in nanoelectronic circuitry, benefiting from their profound subwavelength footprint [23–26]. A debated question arises of how could nanoelectronic performance be enhanced in the light of plasmonics science? As clarified by the field name, in electronics, electrons are the information carriers, with two adverse consequences of low speed and high ohmic loss. This loss causes increase in the power consumption of devices. These factors are in serious contradiction to what is required by the technology. Photonics is an appropriate candidate to solve these challenges. However, it also has a major drawback to device miniaturization, owing to the diffraction limit [4], whereas it is important to consider faster operation, lower power consumption, and miniaturized device size in advanced integrated circuit (IC) design. It is remarkable to understand that miniaturization could play a crucial role in increasing the device speed by itself, as a result of increasing the density in chip and rendering ultradense ICs. According to the above mentioned concerns, plasmonics as a bridge between electronics and photonics is a promising approach to be considered for ultracompact photonic circuits and ultradense data storage [7,25,27–30].

One branch of the plasmonic modes is surface plasmon polariton (SPP), which has evoked enormous interest because of its phenomenal properties of high confinement and broad bandwidth [6,7]. However, SPP structures suffer from ohmic loss effects owing to electron collisions and scatterings. Thereby these structures still need to be improved to decrease the ohmic loss effects. In this way, Boltasseva *et al.* emphasized the use of low-loss plasmonic metamaterials [31]. Moreover, different plasmonic structures have been used to reduce the ohmic loss such as metal-insulator-metal waveguides and slot waveguides [32,33].

In a major advance in 2008, Oulton *et al.* offered a hybrid structure made of a GaAs nanowire separated from a silver surface by a low index dielectric nanogap [34]. The hybrid mode arises from combination of photonic mode in high index dielectric (GaAs) and plasmonic mode on the metal (Ag) interface, occurring in the nanogap. Propagation of the hybrid mode in low index nanogap has significant consequences, such as the interaction of hybrid mode with metal is diminished. Therefore, it results in remarkable decrease of the ohmic loss, whereas nanoscale gap tends to bind up mode into nanodimensions several orders of magnitude below the diffraction limit. This metal-based hybrid structure represents hybrid modes with long propagation length of 40–150 μm and mode confinement ranging from 6×10^3 nm^2 to 6×10^4 nm^2. One of the drawbacks of this metal-based hybrid structure is still the constraint of device miniaturization and also the incompatibility with ultracompact and ultradense IC design.

*hosseinif@shirazu.ac.ir

 ©2023 American Physical Society

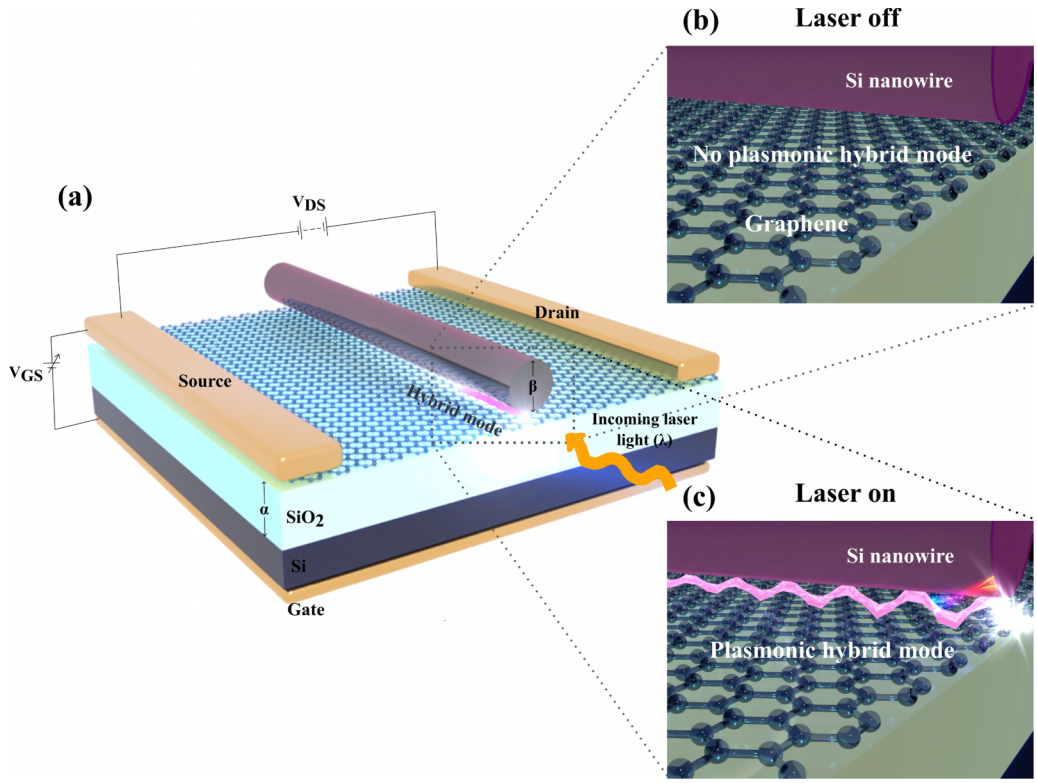

FIG. 1. Schematic of the device structure. (a) Schematic of the hybrid mode field effect transistor. The zoom in view (b) when the laser is off so the plasmonic hybrid mode could not be generated and (c) when the graphene channel and silicon nanowire are illuminated by the laser light in which the plasmonic hybrid mode is observed.

However, 2D plasmonic materials beyond noble metals like graphene could be suitable candidates to render better mode confinement and tunability. Graphene is an atomically thin carbon material with hexagonal lattice structure [35–37]. This material has been the subject of intense debate because of its unique properties and multidisciplinary nature in conjunction with various scientific fields [35,38–43]. The two-dimensional nature of graphene makes it a candidate for device miniaturization [44,45]. Usage of graphene as a plasmonic material enables the achievement of a high degree of field confinement and low optical losses. Moreover, such graphene plasmonic structures show ultrafast response speed because of the ultrahigh carrier mobility of graphene [46,47]. One of the most intriguing merits that has made graphene an instrumental plasmonic material is the wide range of tunability by adjusting the charge carrier density [48–50]. If graphene is employed in a hybrid plasmonic mode (HPM) structure, the design would take advantage of both hybrid mode features and graphene properties together. To the best of our knowledge, most studies which have used graphene in a hybrid mode structure have only focused on graphene tunability rather than its usage as plasmonic material and their structures render modes with huge modal volume and propagation length, which almost are designed for waveguiding [51–53]. These modes are not appropriate candidates for nanoscale ultracompact devices.

In this paper, a combined structure including a graphene field effect transistor (FET) and a silicon nanowire is simulated to study the plasmonic hybrid mode. In such structure, graphene is acting as the plasmonic material and it is also considered as the FET channel. Graphene is a dominant factor in adjusting the hybrid mode parameters by charge carrier density modifications. The significant reason why graphene is employed as the plasmonic material is that it can have a single carrier (electron or hole) channel and two carriers (electron and hole) channel near the charge neutrality point (CNP). Moreover, the graphene inherent properties may shed light on the observation of extremely spatial confinement of the hybrid mode with high tunability. Hence this kind of highly confined mode can be applied to miniaturize devices in ultradense IC design and optical neural networks [25,27,54,55]. Moreover, such a device could be low loss, tunable, and fast response due to the causal role of graphene.

II. METHOD

A FET with graphene channel is simulated by Comsol software to investigate a plasmonic hybrid mode based on its significant carrier transport characteristics. Moreover, in this configuration, a silicon nanowire with high relative permittivity of 12 is considered on top of the single layer graphene with a distance of 2 nm. The schematic of the combined device is shown in Fig. 1. According to this figure, a back gate voltage (V_{GS}) is applied through the silicon dioxide substrate. To observe the plasmonic hybrid mode in this structure, the graphene channel and silicon nanowire are illuminated by a laser light with wavelength of $\lambda = 7$ μm and the hybrid mode is tuned by varying the back gate voltage. In Fig. 2, the analytical curves of carrier density versus the applied gate voltage in graphene are shown according to the following relations. As it can be observed in Fig. 2, from −20 V to −4 V, the graphene

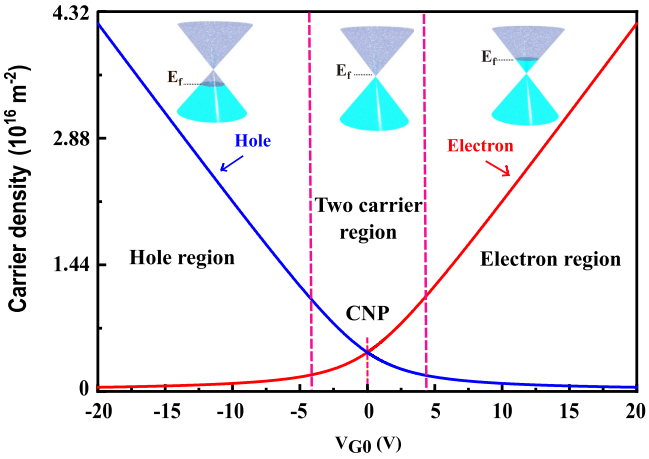

FIG. 2. Electron and hole carrier densities as a function of gate voltage V_{G0}. The Fermi energy level in the Dirac cone is demonstrated for each region.

channel is acting as a single carrier channel based of the holes because the Fermi energy is below the Dirac point. However, from −4 V to 4 V, we can see two carrier channels of electron and hole and, after 4 V to 20 V, the Fermi energy is above the Dirac point; hence electrons can act as the transport carriers.

The behavior of the hybrid mode is significant near the CNP due to the two carrier transportation of graphene. Therefore, there is a requirement to better understand the behavior of graphene near the CNP and the two carrier model should be considered for graphene simulation [56–58]. In the two carrier model, two transport channels are considered and both electron and hole carriers contribute in transport. To accomplish a comprehensive investigation of the plasmonic hybrid mode, we have tailored the effects of gate oxide thickness (α), silicon nanowire diameter (β), and incident laser light wavelength (λ) on the hybrid mode of this structure. The graphene permittivity (ε) was approximated by $\varepsilon = 1 + j\sigma/\varepsilon_0\omega\triangle$ [59]. Where $\triangle$ is the thickness of graphene which is considered 1 nm, σ and ω are graphene conductivity and incident laser light angular frequency, respectively. According to the local random phase approximation of the Cubo formula [60], the conductivity of graphene can be presented in simulation as

$$\sigma_{\text{tot}} = \sum_{i=1}^{2} \sigma_{\text{intra}i} + \sigma_{\text{inter}i}. \tag{1}$$

$i = 1$ refers to electron and $i = 2$ refers to hole and the intraband ($\sigma_{\text{intra}i}$) and interband ($\sigma_{\text{inter}i}$) conductivities are as follows:

$$\sigma_{\text{intra}i} = \frac{2j\,e^2 k_B T}{\hbar^2 \pi(\omega + j\Gamma_i)} \ln\left[2\cosh\left(\frac{\mu_{ci}}{2k_B T}\right)\right], \tag{2}$$

$$\sigma_{\text{inter}i} = \frac{e^2}{4\hbar}\left[\frac{1}{2} + \frac{1}{\pi}\arctan\left(\frac{\hbar\omega - 2\mu_{ci}}{2k_B T}\right)\right] - \frac{j\,e^2}{8\pi\hbar}\ln\left(\frac{(\hbar\omega + 2\mu_{ci})^2}{(\hbar\omega - 2\mu_{ci})^2 + (2k_B T)^2}\right), \tag{3}$$

where $\hbar$ is the reduced Planck's constant, e is the elementary charge, k_B is the Boltzmann constant, and T introduces the temperature which is considered 300 K. Graphene Fermi energy (chemical potential) is $\mu_{ci} = \hbar v_F(\pi n_i)^{1/2}$ and its relation with relaxation time (τ_i) and carrier scattering rate (Γ_i) is as below:

$$\tau_i = 1/\Gamma_i = \mu_i \mu_{ci}/\left(e v_F^2\right). \tag{4}$$

$v_F \approx 10^8$ cm/s is the Fermi velocity, n_i introduces the charge carrier density, and μ_i is the carrier mobility [61]:

$$\mu_i = \frac{10en^*}{\pi\hbar n_i n_{\text{imp}}}. \tag{5}$$

The sources of charge carrier densities in the graphene channel are classified as source-drain and gate-induced carrier densities (n_{CV}) [62], thermally generated carrier density (n_{th}), residual carrier puddle density (n^*), and the density of electrostatic spatial inhomogeneity (n_{imp}). For the SiO_2 substrate, $n_{\text{imp}} = 8.855 \times 10^{11}$ cm^{-2} and $n^* = 0.297\ n_{\text{imp}} = 2.63 \times 10^{11}$ cm^{-2} [61]:

$$n_{CV} = n_2 - n_1 = -(C/e)(V_{G0} + V_{DS}/2), \tag{6}$$

$$n_{th} = (\pi/6)(k_B T/\hbar v_F)^2, \tag{7}$$

where $C = \varepsilon_{SiO_2}/\alpha$ is the substrate capacitance per unit area, ε_{SiO_2} is the substrate permittivity, α is the gate oxide thickness, $V_{G0} = V_{GS} - V_0$ is the gate voltage referenced to the Dirac point voltage (V_0), and V_{DS} is the drain-source voltage. The carrier density of electron or hole is acquired by

$$n_i \approx \tfrac{1}{2}\left[\pm n_{CV} + \sqrt{{n_{CV}}^2 + 4{n_0}^2}\right]. \tag{8}$$

The plus sign corresponds to electrons, the minus sign refers to holes, and n_0 is the minimum carrier density at the Dirac point (CNP):

$$n_0 = \left[(n^*/2)^2 + {n_{th}}^2\right]^{1/2}. \tag{9}$$

Carrier densities of electron and hole as a function of gate voltage are demonstrated in Fig. 2, in which the curves are drawn according to formula (8). It can be observed that, for graphene, we can recognize three specific regions of hole—two carrier and electron region.

III. RESULTS AND DISCUSSION

Two main parameters are employed to describe an optical mode behavior. One of them is the propagation length (PL) and the other is the normalized mode area (A/A_0), where A refers to the modal area and $A_0 = \lambda^2/4$ is the diffraction-limited area in the free space [34]. The modal area (A) is defined as the effective area to which the mode could distribute the same energy through a uniform field. The normalized mode area is the most well-known criteria for assessing the mode confinement.

In order to gain insight into the correlation between the mode character and the type of structure, three different structure models are classified, such as photonic, plasmonic, and hybrid structures (Fig. 3). In all three structures, α (gate oxide thickness) = 100 nm, β (nanowire diameter) = 50 nm, and λ (incident wavelength) = 7 μm are considered. The first classification is considered as photonic structure in which there is only a silicon nanowire in the air [Fig. 3(a)]. In this

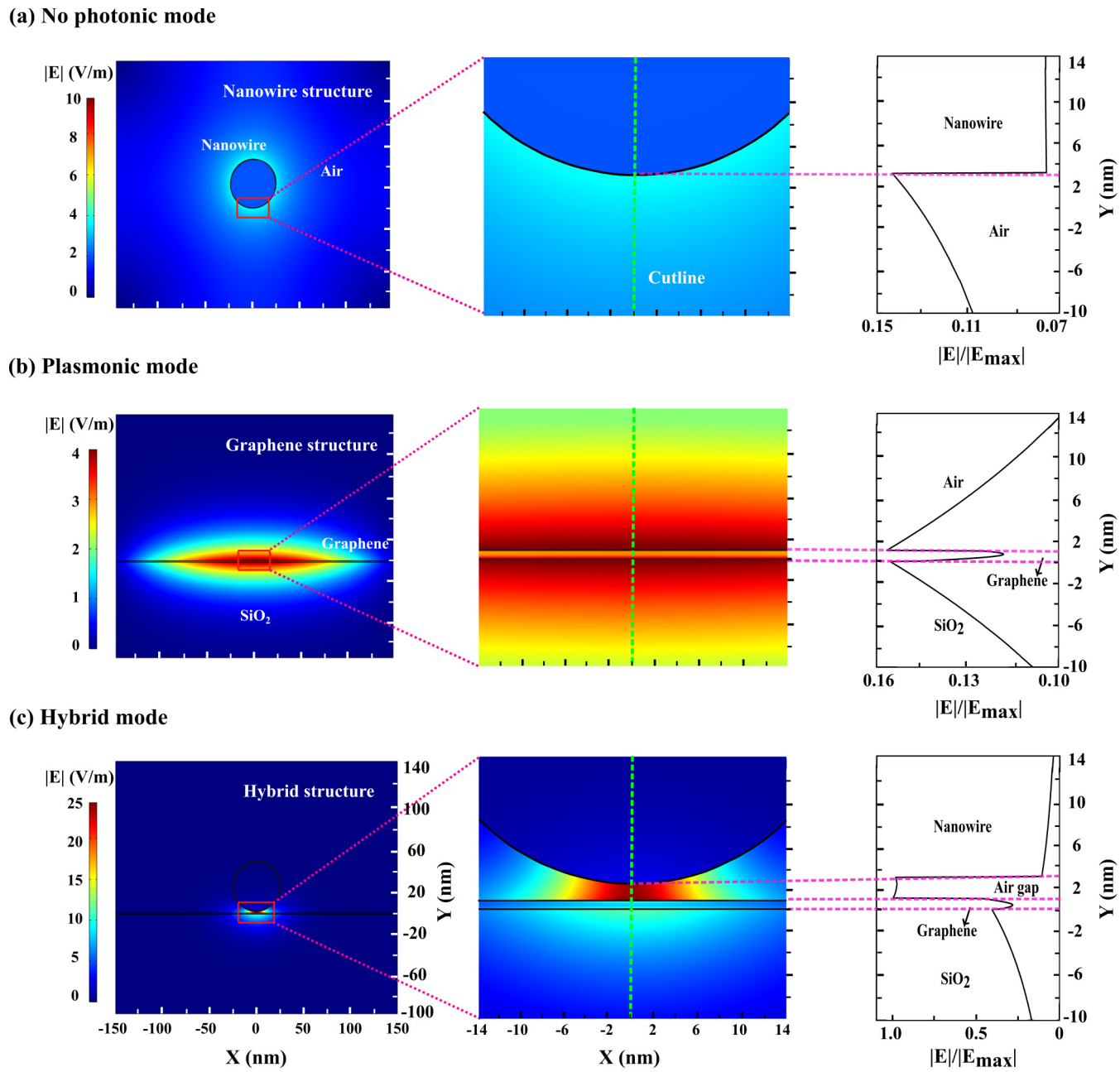

FIG. 3. Comparison of the (a) photonic, (b) plasmonic, and (c) hybrid structure modes. In each part, the left figure is the electric field magnitude $|E|$ of the mode and its rectangular section is zoomed in the middle figure. For better comparison, the right plots represent the electric field magnitude $|E|$ on the specified vertical cut lines, which is normalized to the maximum value $|E|_{\max}$ of the hybrid mode.

case, the diffraction limit prevents photonic mode constitution in the nanowire, because of its small diameter. However, in Fig. 3(a), a circular halo-shape mode is observed around the nanowire due to permittivity contrast and continuity of a normal displacement vector at the air-silicon interface. The second classification is defined as the plasmonic structure in which a graphene monolayer is located on top of the gate oxide in a FET [Fig. 3(b)]. It can be seen from Fig. 3(b) that a plasmonic mode is formed on graphene.

The combination of graphene FET and silicon nanowire with an air gap of 2 nm is considered as the third case, as shown in Fig. 3(c). In such a hybrid structure, there are three capacitorlike effects between graphene sheet and back gate, between drain and source, and between the nanowire and graphene. The main reason to observe the plasmonic hybrid mode is the interaction of nanowire interface polar charges and surface plasma oscillations of graphene, which leads to capacitive coupling between graphene and nanowire. This capacitive coupling entails the hybrid mode creation in the gap region between graphene and nanowire.

Figures 4(a) and 4(b) present A/A_0 and PL versus V_{G0} for the plasmonic and hybrid modes of Fig. 3. Figure 4(b) shows that, by applying gate voltage, the PL of the plasmonic mode changes in the range between 5.3 nm and 10.9 nm; in contrast the PL reduced to the range of 4.5 nm to 8.9 nm for the hybrid mode. However, as observed in Fig. 4(a), A/A_0 in the hybrid

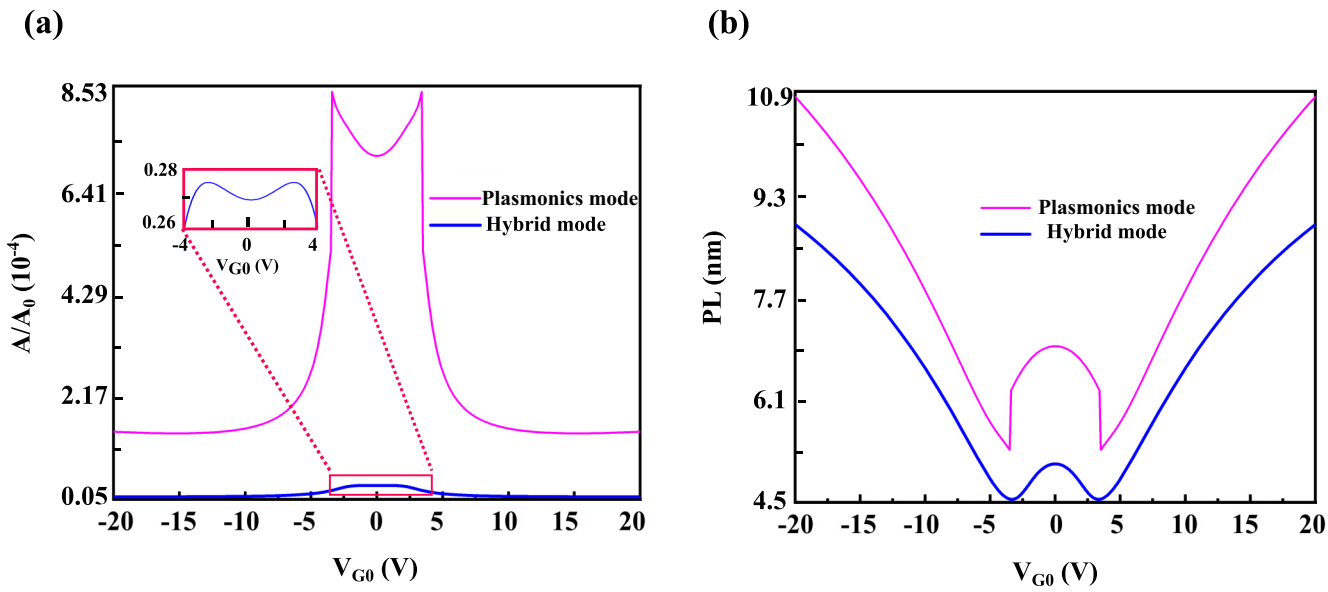

FIG. 4. Comparison of the plasmonic and the hybrid mode parameters. The plots of (a) normalized mode area A/A_0 and (b) propagation length PL versus gate voltage V_{G0} for the plasmonic and the hybrid modes. The inset of (a) shows the curve trend of the hybrid mode near the charge neutrality point.

mode is suppressed and its value as a comparison is 30 times smaller than the plasmonic mode A/A_0, because of high confinement of the hybrid mode. Moreover, the plasmonic mode is elongated in one dimension along x direction, whereas the hybrid mode also has a lateral confinement and is limited in two dimensions along x and y directions.

This strong energy confinement in the gap between the nanowire and graphene is explained by several reasons. When the structure is illuminated by laser light, the perpendicular component of electric field for both graphene-air and air-nanowire interfaces is dominant in both uncoupled surface plasmon and cylinder geometries and also the high index contrast effect is instated in both interfaces. Therefore, the condition of normal displacement field continuity results in strong confinement in the nanoscale gap. In addition, the curvature of nanowire geometry improves the lateral confinement and is an advantage in 2D confinement realization [Fig. 3(c)].

In addition, in Figs. 4(a) and 4(b), for both plasmonic and hybrid modes, the trend of plots is almost similar. For both modes, from −20 V to −4 V we have single carrier channel of hole and after 4 V to 20 V a kind of electron carrier transportation exists in which the single carrier channel in both electron and hole regions leads to a linear behavior. However, for both modes, a nonlinearity is observed from −4 V to 4 V which is due to the two carrier channel in the presence of hole and electron carriers near the CNP. Meanwhile, graphene proximity with nanowire in the hybrid structure leads to the hybrid mode affected by its photonic nature and therefore moderates the graphene emanated sharp nonlinearity to a kind of sine wave behavior. Although the nonlinearity near graphene CNP has been observed experimentally in research by Song *et al.* [63], in this manuscript we explain the details of physics behind this nonlinearity analytically.

As mentioned above, the nonlinear treatment near the CNP is due to the two-carrier model in graphene. The nature of the two-carrier model near the CNP in graphene is due to four important effects of electron-hole puddling, weak localization, transportation, and recombination [64,65]. The physics governing the formalism in our analytical simulation includes these effects. In the next paragraph these effects will be described in greater detail.

The backbone physics of the puddling effect is as follows. When a charge carrier is surrounded by other charge carriers, due to the screening effect, that carrier will be less affected by its environment [66]. As the carrier density decreases, the screening effectiveness is reduced. As shown in Fig. 2, near the CNP, the total carrier density is minimum; hence the graphene sheet is strongly affected by environmental disorder factors. These inhomogeneity factors could be the random distribution of unintentional quenched charged impurity centers in surrounding and substrate interface roughness. Moreover, the intrinsic structural ripples in graphene could be another inhomogeneity source [64]. Based on theoretical and experimental research, it has been proved that the disorder-induced potential fluctuations break up the carriers' landscape into electron-hole puddles.

The main reason for nonlinearity in the graphene sheet is weak localization, which occurs as a consequence of the disorder distribution of puddles. In other words, carriers are subjected to different scattering mechanisms which localize them and affect their transportation features. The physical puddle concept develops a theory for graphene transport using a self-consistent approximation [61].

In order to better understand the behavior of plasmonic hybrid mode, we study various effects such as changing the gate oxide thickness (α), the nanowire diameter (β), and the wavelength of incident laser light (λ) on the hybrid mode parameters.

Figures 5(a)–5(c) show the variation of A/A_0, PL, and the PL rate (first derivative of PL) versus the applying gate voltage V_{G0}, where $\beta = 50$ nm and $\lambda = 7$ μm. According to Fig. 5(a), the modal area of the graphene hybrid mode is about 10^5 times

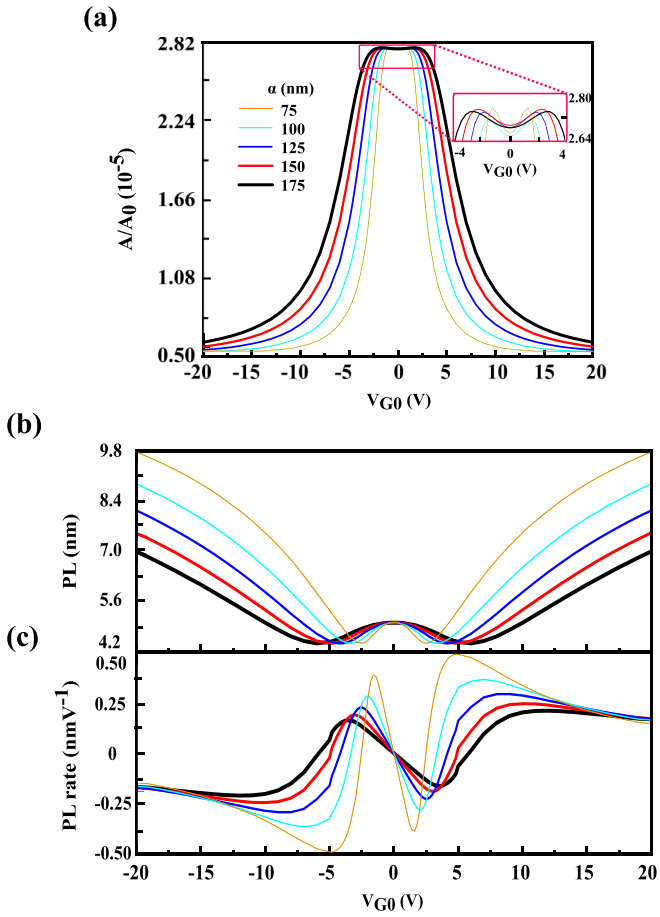

FIG. 5. Dependence of the hybrid mode parameters on gate voltage V_{G0} for different gate oxide thicknesses α. (a) The Normalized modal area A/A_0, (b) propagation length PL, and (c) the first derivative of propagation length (PL rate) as functions of gate voltage V_{G0} for different values of gate oxide thickness α. The inset is the zoom of the nonlinear behavior near the charge neutrality point.

smaller than the area of a diffraction limited spot [ranging from $\lambda^2/(8 \times 10^5)$ to $\lambda^2/(1.5 \times 10^5)$]. The effective area of observed nanometer-scale high-intense energy mode in this work could be three orders of magnitude smaller than the modal area of similar hybrid structure as shown in other work by Oulton *et al.*, in which a silver metal was used to support plasmons in their study [34]. Figure 5(b) illustrates that the observed hybrid modes have low PL (ranging from 4.2 nm to 9.8 nm), which is an advantage. Low PL in addition to an ultraconfinement feature presents a nanoscale volume hotspot that is essential for compact devices.

All plots of Fig. 5 have a linear behavior at single carrier regions of electron or hole, while in the CNP area the dominant observation is nonlinearity. As can be seen from Fig. 5(a), A/A_0 from -20 V to -4 V is increased; however, from 4 V to 20 V in the electron region, A/A_0 is decreased. Simultaneously the PL is decreased from the hole region to the CNP region and, after 4 V, the PL in the electron region is increased; hence lower PL in the CNP region is the evidence for existence of the puddling effect and weak localization near the CNP [Fig. 5(b)]. Moreover, the PL rate near the CNP shows an intense oscillating trend as a comparison in the hole or electron region [Fig. 5(c)].

To explain more about Fig. 5(a), by increasing the gate voltage from 4 V to 20 V in the electron region, the charge carrier density will increase; therefore, the association of the plasmonic nature of the hybrid mode enhances thus affecting the mode to be more confined (Fig. 2). On the other hand, from -4 V to -20 V, which is the hole side, the same thing is also happening. In addition, for both single carrier regions, by changing α from 175 nm to 75 nm, for a constant value of gate voltage, e.g., $V_{G0} = 10$ V, the carrier density increases from 1.27×10^{16} m^{-2} to 2.89×10^{16} m^{-2}, which causes more confinement for the hybrid mode.

In order to justify the behavior of PL curves, according to the previous report [67], the PL of plasmons on the graphene surface is proportional to the Fermi energy level. Therefore, by changing the gate voltage from CNP region to the single carrier regions either electron or hole, the carrier density and the Fermi energy level are increasing and the PL also increases. As said before, in single carrier regions for a constant voltage, by changing α from 175 nm to 75 nm, the carrier density increases [formula (6)]; thus PL will increase. At the same time, by decreasing α, the electric field generating between the graphene and the gate oxide will enhance as a capacitorlike effect. The stronger field affects the plasmons on

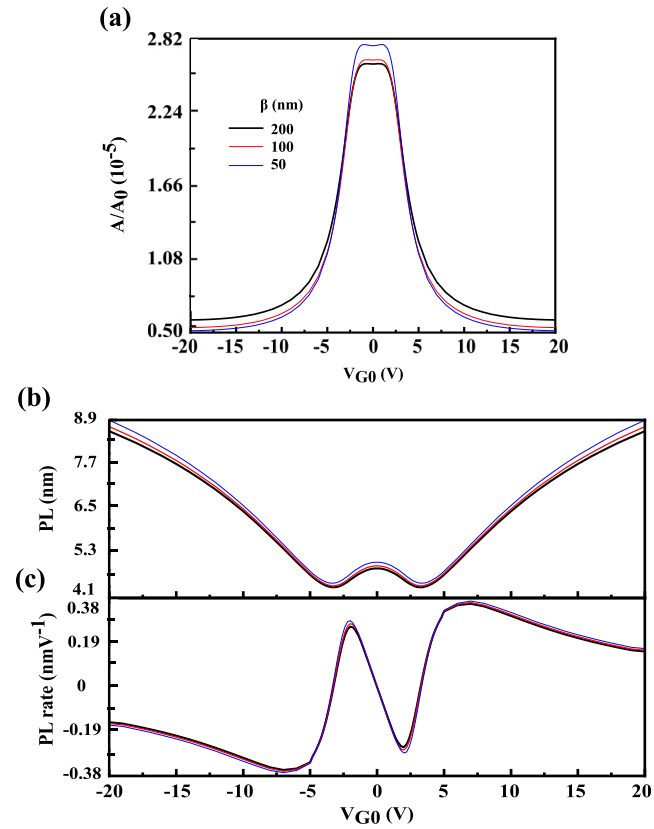

FIG. 6. Influence of nanowire diameter β on the hybrid mode parameters. (a) The normalized modal area A/A_0, (b) propagation length PL, and (c) the first derivative of propagation length (PL rate) as functions of gate voltage V_{G0} for different values of nanowire diameter β.

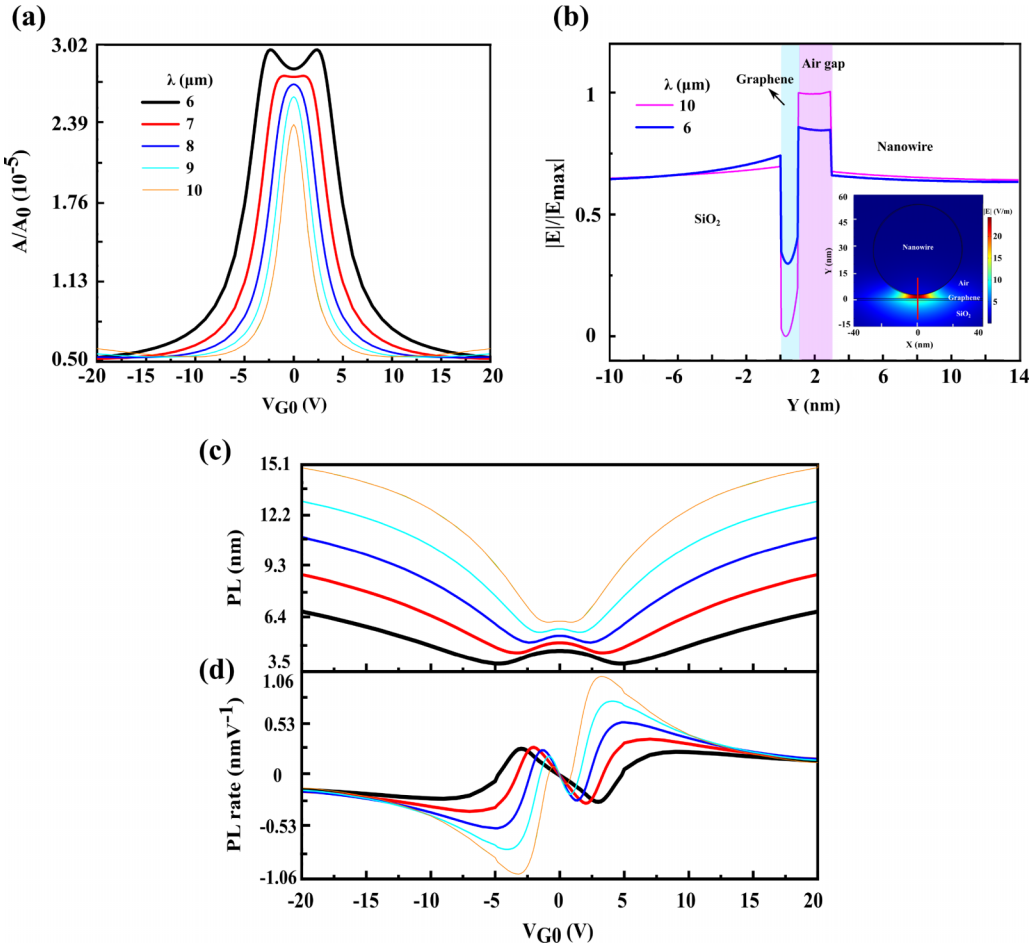

FIG. 7. Effectiveness of the hybrid mode parameters from different wavelengths λ and their relation to the electric field distribution in the structure. (a) The normalized modal area A/A_0 versus the gate voltage V_{G0} for different values of wavelengths λ. (b) The electric field magnitude of the hybrid mode on the specified vertical cut line in the inset, for λ = 10 μm and λ = 6 μm at $V_{G0} = 0$ V, which is normalized to the maximum value. (c) Propagation length PL and (d) the first derivative of propagation length (PL rate) as functions of gate voltage V_{G0} for different wavelengths λ.

graphene more efficiently and presents better response. Figure 5(c) confirms that the $\alpha = 75$ nm plot has more effective response with respect to variation of V_{G0} than other plots. It is noteworthy that high responding is an essential factor for sensing applications [14]. Albeit the character of observed modes in the entire region from −20 V to 20 V is hybrid, in electron and hole regions the plasmonic nature of the hybrid modes is significant.

We have done the same analytical study in the structure while changing the diameter of the nanowire (β) from 50 nm to 200 nm without changing the graphene FET structure and laser wavelength (where $\alpha = 100$ nm and λ = 7 μm). In general, A/A_0, PL, and PL rate in Fig. 6 have the same trend as Figs. 5(a)–5(c) and, by changing β, we do not see any significant changes. The reason is that the hybrid mode has been created by the correlation between plasmons on graphene and the polarization charges of the nanowire lower surface, which is curved; hence the effective interaction surface is low enough even for larger diameters. Furthermore, the nanowire diameter does not affect the graphene carrier density, mobility, or other carrier transportation properties.

Figure 7 illustrates the influence of the incident laser light wavelength (λ) on the hybrid mode features (where $\alpha = 100$ nm and $\beta = 50$ nm). By considering the plots of A/A_0 and PL [Figs. 7(a) and 7(c)], it is clarified that, for larger λ, the modes appear to be low affected by two carrier character of the graphene, because they reveal weak nonlinear behavior near CNP. In order to identify the cause of weak nonlinear behavior near CNP, the normalized magnitude of electric field ($|E|/|E_{\max}|$) on the specified vertical cut line is demonstrated for λ = 6 μm and λ = 10 μm at $V_{G0} = 0$ V [Fig. 7(b)]. By comparing the two plots of λ = 6 μm and λ = 10 μm, it is obvious that the electric field for λ = 6 μm is more intense than λ = 10 μm inside the graphene. It means that, for the incident laser at λ = 6 μm, the mode has more interaction with graphene; hence it could be more affected by the graphene intrinsic features.

It is clear that the λ = 6 μm mode has lower intensity in gap and its energy distributed in the graphene and the gate oxide more than the mode with λ = 10 μm, which results in increasing the modal area. To explain the PL trend, as reported before [67], the propagation length of plasmons on

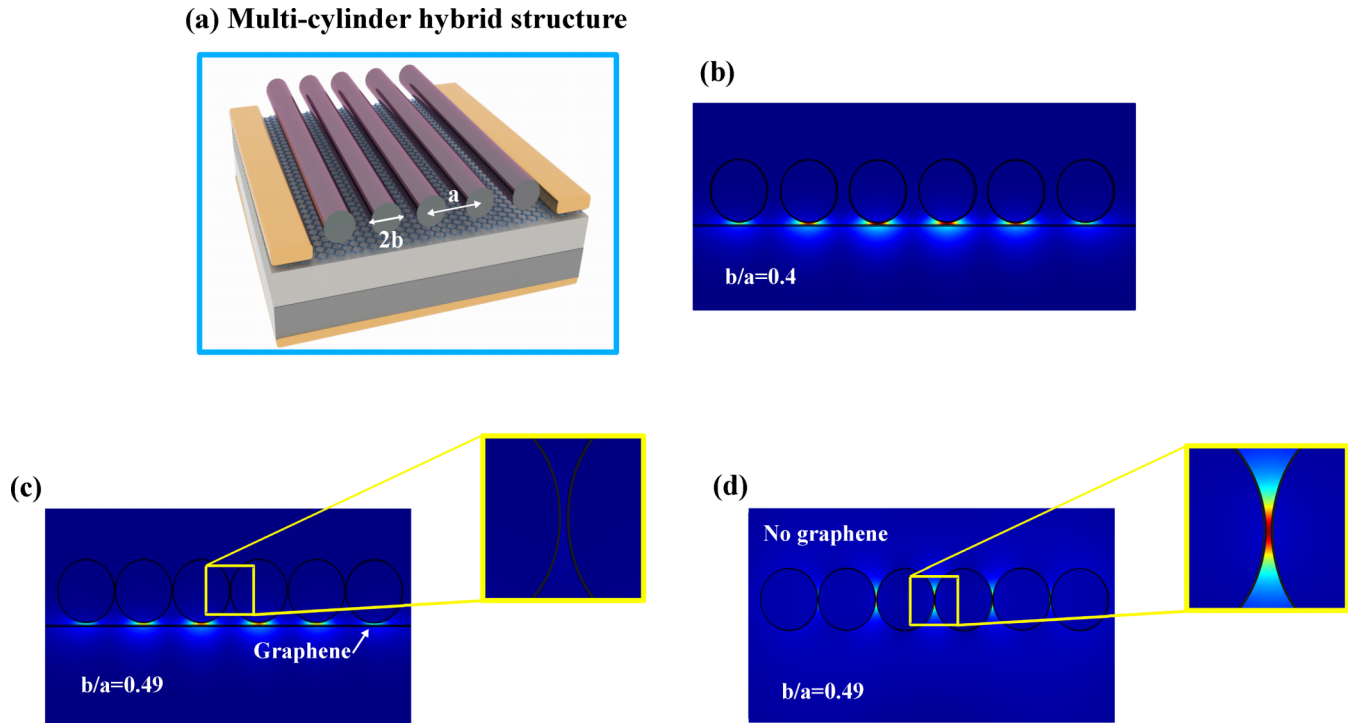

FIG. 8. Hybrid multicylinder structure. (a) The schematic picture of a multicylinder hybrid transistor. (b), (c) The electric field distribution of the hybrid multicylinder structures of $b/a = 0.4$ and $b/a = 0.49$, respectively. (d) The electric field distribution of multicylinder photonic structure.

graphene is proportional to λ. Because the variation of V_{G0} changes the plasmonic nature of the hybrid mode, so the hybrid modes with larger wavelength have longer propagation length [Fig. 7(c)]. The plots of PL derivative [Fig. 7(d)] illustrate that increasing λ leads to decreasing the effective response of the hybrid mode near the CNP.

By observing the high confinement of the hybrid mode and also tuning the PL in the nanometer range, this kind of nanostructure could be suggested for nanoscale energy storage [68,69], optical neuromorphic computing, and high density nanoelectronic devices [25,27,54,55].

IV. MORE INVESTIGATIONS WITH OTHER NANOWIRES

A. Multicylinder

One of the most important concepts in integration of electronic components is the unwanted interactions between components and the maximum reduction of these types of interactions is a demand. To investigate this issue, a structure containing multicylinders is considered in which, according to Fig. 8(a), they are placed next to each other with the same distance. The goal is to see if the hybrid modes tend to the continuum optical bound states of the periodic array of silicon nanorods. Figure 8(a) shows an array of cylinders (CYLs) in the transistor hybrid structure which are illuminated by the laser beam from the cross section as before. The distance between nanorods is denoted by a and their diameter is specified by $2b$.

The field distribution of the array structure with $b/a = 0.4$ in $V_{G0} = 20V$ could be seen in Fig. 8(b). As the field distribution shows, no optical bound state is formed parallel to the nanorods. It seems that the strong coupling between the plasmonic and photonic modes has prevented the formation of parallel bound states between nanorods. Although this reason seems logistic, for more confidence, another array structure with ratio $b/a = 0.49$ was considered in which, for $b = 25$ nm, two CYLs are very close to each other (about 1 nm). The field distribution in this case [Fig. 8(c)] shows that, despite the very small distance between CYLs, the hybrid coupling is still so strong that it is not possible to witness the formation of bound states. The strong proof of this claim is the structure of Fig. 8(d) in which the graphene layer (the plasmonic material) is omitted. In this case in which the plasmonic photonic has no role in the formation of the mode, the optical bound state in the continuum is allowed to appear. It is worth saying that, if the nanowire diameter is high enough to allow the formation of a photonic mode inside the CYLs, interesting layouts of the optical field can be observed in the array [70]. This section has a very important result, in which it is possible to place adjacent components of such structures too close to each other, while the cross talk between them is completely negligible. This factor, in addition to the small size of the mode, could be the key points for the realization of high-density photonic integration.

B. Multilayer cylinder

In this section we want to investigate the effect of a multilayered nanorod on the hybrid mode. Five cylindrical layers (shells) have been considered which are concentric and have the same thickness (the outer diameter of the last layer is

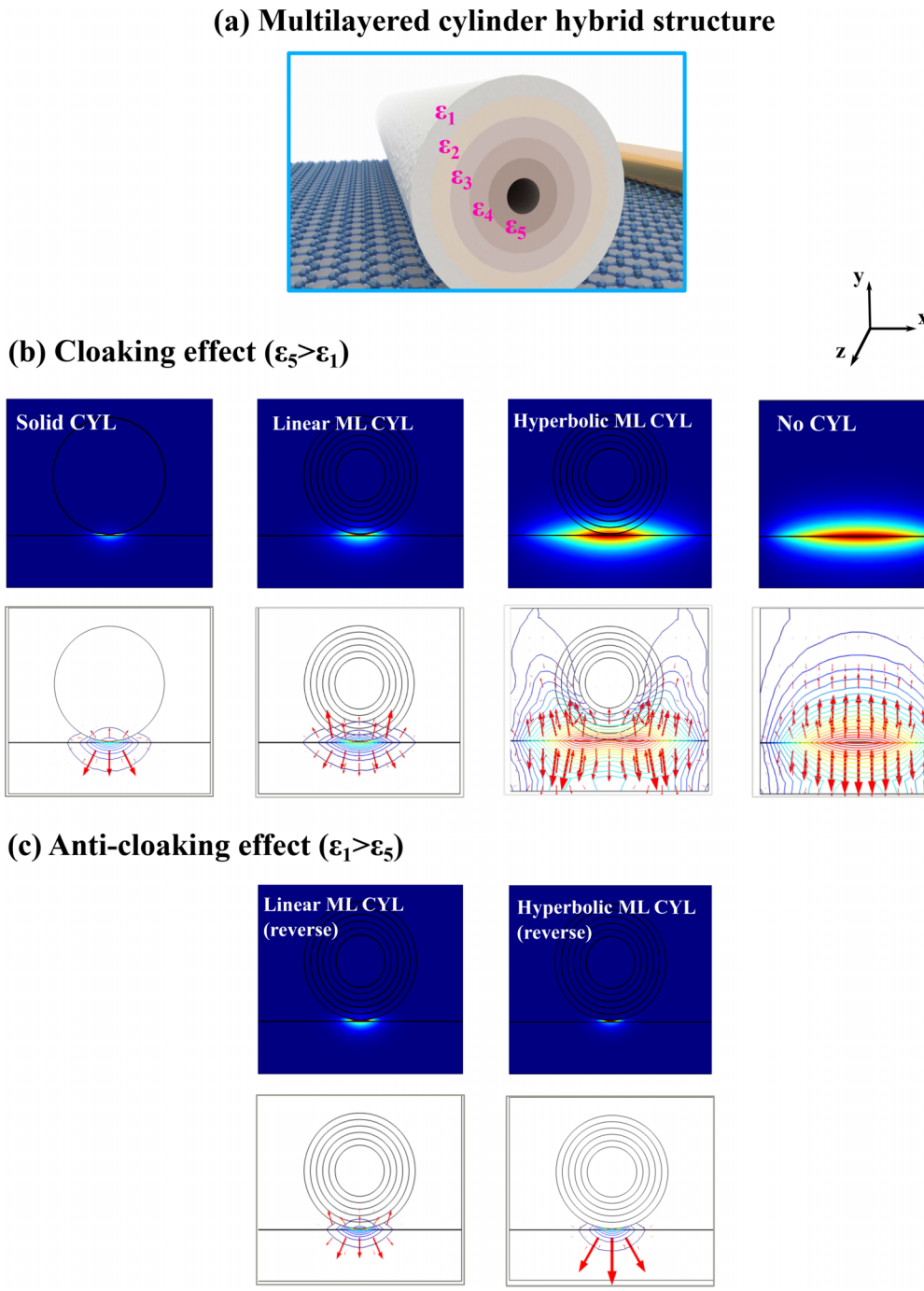

FIG. 9. Multilayered cylinder hybrid structure. (a) The schematic picture of the five layer CYL hybrid structure. (b), (c) The electric field distribution (top row) and contours and arrows (bottom row) for the cloaking effect and anticloaking effect, respectively.

113 nm and the inner diameter of the first layer is 50 nm). The schematic image of this multilayer cylinder (ML CYL) structure has been shown in Fig. 9(a). Two arrangements of the layers of dielectric constant values are considered in such a way that in one arrangement the dielectric constants increase linearly ($\varepsilon_i = 3.22, 5.44, 7.66, 9.88, 12.1$) and the dielectric constants of the other arrangement increase hyperbolically ($\varepsilon_i = 1.25, 1.66, 2.47, 4.85, 128$). The selection of these dielectric constants relies on an effective medium approach to realize an effectively anisotropic permittivity. So these structures are expected to render some cloaking concept [71].

The images of field distribution (top row), contours, and arrays (bottom row) in $V_{G0} = 20V$ are shown in Fig. 9(b). For better comparison, the field distributions of the monolayer graphene (right) and the hybrid structure with solid CYL (left) have been also demonstrated. The comparison of the fields has some interesting points. In the field distributions of ML CYLs, one can see the penetration of the field inside the layers which

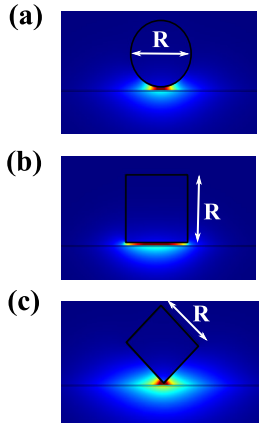

Different nanorods	R (nm)	A/A0 (E-6)	PL (nm)
(a)	10	9.50	7.99
	50	5.14	8.89
(b)	10	5.96	7.31
	50	6.62	7.96
(c)	10	4.53	9.49
	50	1.61	10.30

FIG. 10. Mode parameters and shape of the structures with different cross sectional shape of the nanorod. (a), (b), (c) The mode parameters of circular, square, and rhomboid cross section nanorod structures, respectively.

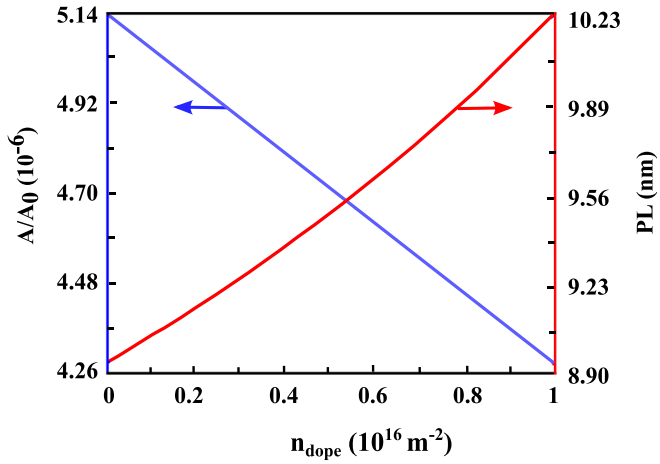

FIG. 11. Effects of doping on the mode parameters. The plots of normalized mode area A/A_0 and propagation length PL parameters versus the doping carrier n_{dope}.

leads to field extension. The field distribution diagrams could partially show the cloaking effect in which this effect seems stronger in the hyperbolic case. However, the comparison of the bottom row images provides a better understanding of the cloaking effect. In these plots, the contours of electric field norm have been shown; moreover, the plots contain arrays in which their x component is E_x and y component represents E_y. It is clarified from comparing the contours and arrays that scatterings from hyperbolic ML CYLs are in such a way that it seems that the ML CYL has become effectively invisible. The field distribution and contours of the hyperbolic ML CYL tend to mimic the field shape of the structure with no CYL [Fig. 9(b), right]. which is approaching the concept of cloaking.

Bear in mind that the cloaking leads to field extension and so, decreasing the mode confinement, it can be expected that the reverse arrangement of dielectric constants in ML CYLs (i.e., anticloaking effect) will improve the mode confinement. This issue is clearly evident in the plots of field distribution and contours related to reverse ML CYLs of Fig. 9(c). In the reverse ML cases, a better confinement is obtained than the first ML structures of Fig. 9(b). Even the structure of reverse hyperbolic ML CYL has more confinement—about 1.5 times—compared to the solid CYL structure. However, their contour and array plots are very similar to each other.

C. Nanorod shape

To investigate the effect of nanorod shape, in Figs. 10(a)–10(c), the parameters of mode have been calculated for different nanorods in $V_{G0} = 20V$ and their electric field distribution has been shown. As indicated in the figures, the size characteristic parameter, R, is different for each nanorod. According to the table inserted in the figure, the nanorod structure with rhombus cross section presents higher confinement; however, it should be considered that the calculation of the field in sharp points by the software may not be accurate enough.

V. MORE INVESTIGATION OF THE PLASMONIC MATERIAL (graphene)

A. Carrier doping

We want to examine the effects of chemical doping on the hybrid mode parameters. Figure 11 shows the plots of A/A_0 and PL for different values of n_{dope} (doping carrier density) in $V_{G0} = 20V$. As explained before, increase of the carrier density both by doping or applying a gate potential leads to a plasmonic nature increment of the hybrid mode, which results in confinement increasing. Moreover, an increase in doping is accompanied by an increase in Fermi energy level, which increases PL accordingly.

B. Step discontinuity

One of the excellent properties of graphene is the ability for local variation of its Fermi energy by doping or applying a gate voltage. This feature results in position dependent surface conductivity, which is accompanied by tunability of its properties [72,73].

To investigate the effects of inhomogeneity caused by abrupt termination of graphene, we consider the graphene layer by a piecewise step discontinuity profile. For a more detailed analysis, two general cases of symmetric and asymmetric discontinuity are simulated. Figure 12(a) shows the schematic picture of the symmetric case in which the middle layer is specified by the length of P. In the structures of Fig. 12(b), the properties of the middle layer are chosen in such a way that $\text{Re}(n_{\text{middle}}) < \text{Re}(n_{\text{sides}})$ and $\text{Im}(\varepsilon_{\text{middle}}) > \text{Im}(\varepsilon_{\text{sides}})$. Conversely, in the structures of Fig. 12(c), the properties are $\text{Re}(n_{\text{middle}}) > \text{Re}(n_{\text{sides}})$ and $\text{Im}(\varepsilon_{\text{middle}}) < \text{Im}(\varepsilon_{\text{sides}})$. The results show that, in general, creating discontinuity does not have any effect on improving the mode concentration. However, the piecewise discontinuity profile could affect the overall shape of the mode. The values of P vary in the steps of 5 nm. In Fig. 12(b), for the P values in the interval of 5–35 nm, the mode is like the previous hybrid modes [a sample of this interval mode is presented in Fig. 12(b), left]. From 40 to 85 nm, the hybrid mode is formed,

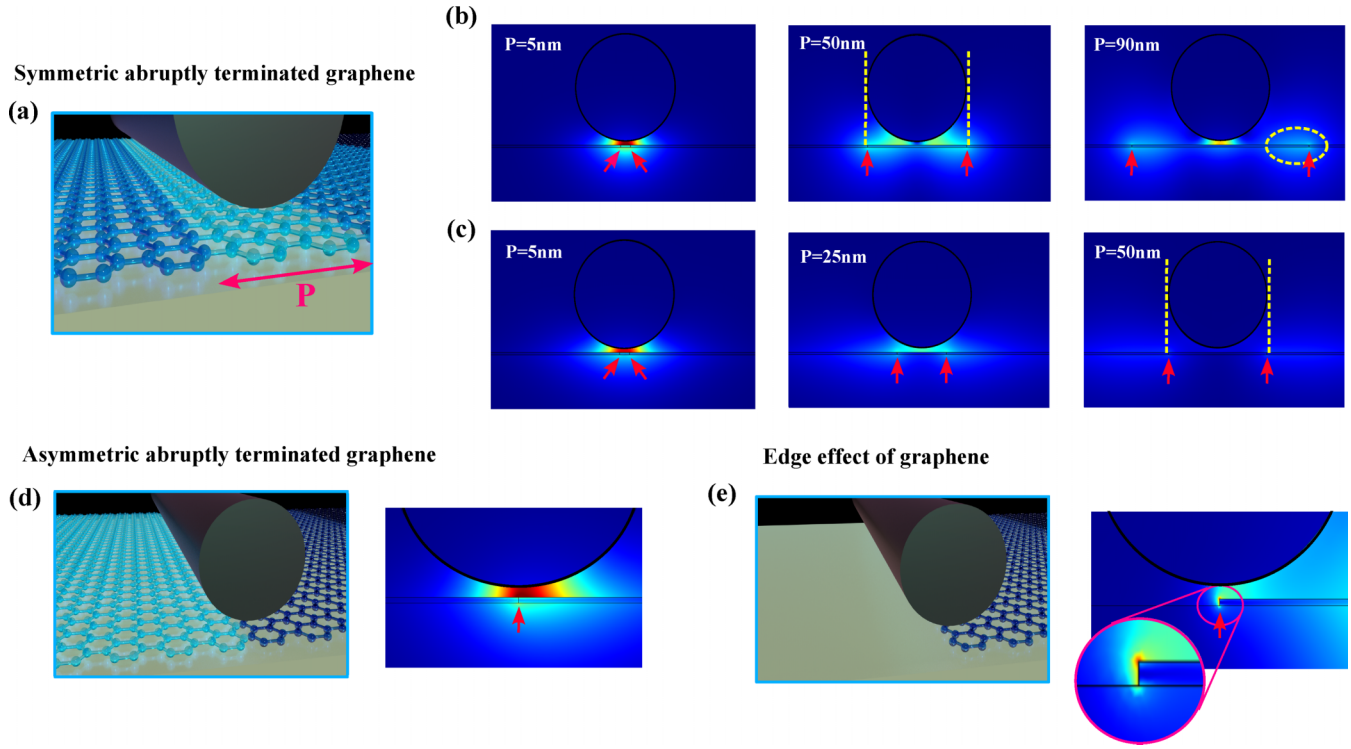

FIG. 12. Hybrid structure with abruptly terminated graphene. (a) The schematic picture of the symmetric structure. (b), (c) The electric field distribution of the symmetric structures in which the middle layer of graphene has higher (top row) and lower metallic features (bottom row) than the side layers, respectively. (d), (e) The schematic picture and the electric field distribution of the hybrid structure with asymmetric abruptly terminated graphene and the structure with edge effect of graphene, respectively. In all of the parts, the red arrows show the discontinuity locations.

but it tends more to the discontinuity points, so a gap in the center of the mode is observable [Fig. 12(b), middle] and, for P values from 90 nm to above, in addition to the hybrid mode in the center, some field accumulation is observed at the discontinuity locations, which decreases the confinement drastically [Fig. 12(b), right].

In the reverse case [Fig. 12(c)], for $P = 5$–15 nm, the hybrid mode is formed so that its confinement decreases by increasing P [Fig. 12(c), left and middle]. Ultimately, for $P = 30$ nm to above, there are only weak accumulations of field around the discontinuity sites for which practically we could say that we will not have any mode confinement in this situation [Fig. 12(c), right]. It is trivial that for the two symmetrical cases mentioned [Figs. 12(b) and 12(c)], for very large values of P, the hybrid mode forms as before and the discontinuity is not sensible. In Figs. 12(b) and 12(c), one can see the effects of scattering by abrupt discontinuity in which these effects are more prominent in Fig. 12(b), middle and right; the reason could be $\mathrm{Re}(n_{\mathrm{middle}}) < \mathrm{Re}(n_{\mathrm{sides}})$. The other point is that, in structures of Fig. 12(b), more confinement could be seen because the middle layer of Fig. 12(b) has more metallic features [$\mathrm{Im}(\varepsilon_{\mathrm{middle}}) > \mathrm{Im}(\varepsilon_{\mathrm{sides}})$] than the side layers.

Figure 12(d) shows the schematic picture and field distribution for the case of asymmetric step distribution in which the conductivity profile has been governed by a Heaviside step function. In this case, the general properties are $\mathrm{Re}(n_{\mathrm{left}}) < \mathrm{Re}(n_{\mathrm{right}})$ and $\mathrm{Im}(\varepsilon_{\mathrm{left}}) > \mathrm{Im}(\varepsilon_{\mathrm{right}})$. It seems that, in this structure, the mode tends to the right, which is because the mode experiences a higher concentration in the left side due to the higher metallic property of its graphene layer. Figure 12(e) is a subset of structure in Fig. 12(d), which studies the effect of the graphene edge and it looks like the laser beam represented in the vicinity of the corner of graphene. As the inset of Fig. 12(e) demonstrates, in this structure, the hybrid mode has a strong tendency to the plasmonic mode, which is due to the effect of graphene abrupt edge which concentrates the mode on the graphene edge.

C. Ultra-long-range hybrid mode by twisted graphene

The last section is associated to usage of twisted bilayer graphene (TBG) instead of graphene monolayer, as the plasmonic material. In TBG, a layer of graphene is placed on the other layer while twisted with respect to it. Hybridization between the Dirac cones of graphene layers leads to new electronic properties; the most significant feature is that, for special twisted angles in TBGs, namely "magic angles," the transition to the superconductivity regime will take place [74,75]. Two dimensionality of TBGs makes its superconductivity more outstanding. Figure 13(a) presents a schematic picture of the hybrid transistor with a TBG and the details of TBG are visible in its inset. It could be seen that, by twisting the graphene layers under the angle of θ, one can see the hexagonal lattice of graphene which is governed by a larger honeycomb lattice. This lattice has a larger honeycomb moiré pattern. As it was said, the TBG could gain the phase of superconductivity and its resistance trends to zero. So we

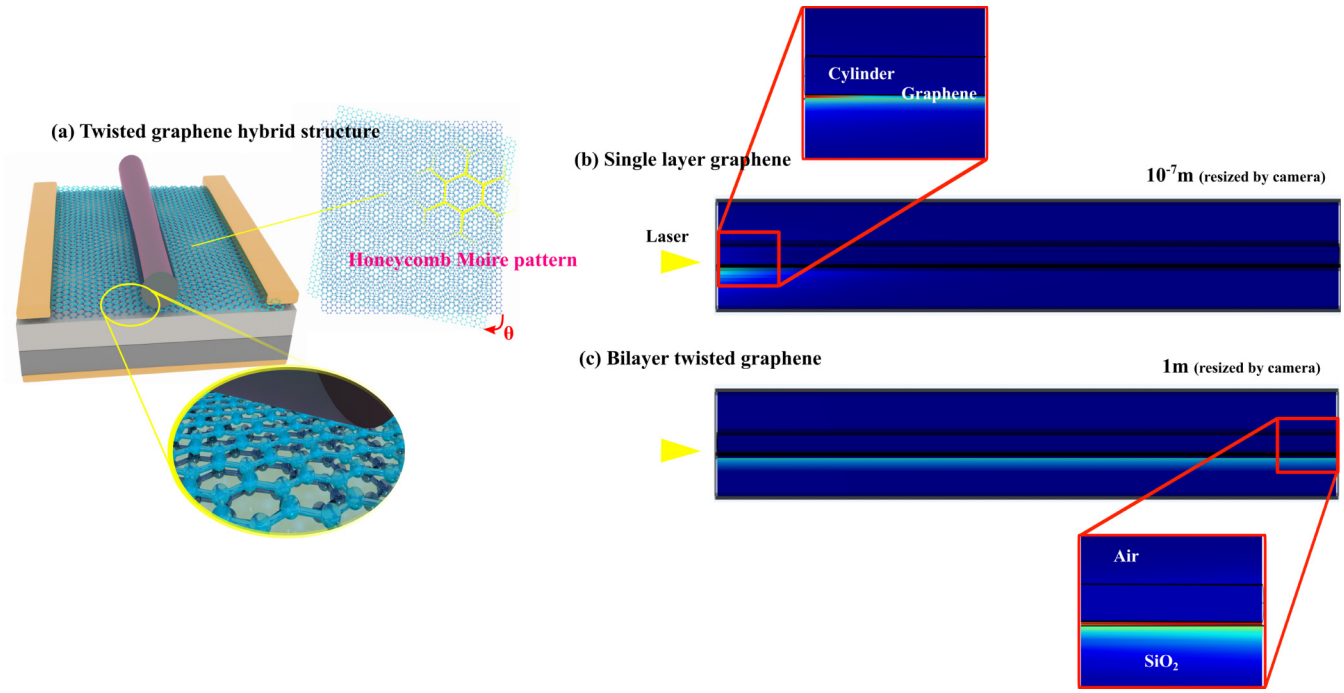

FIG. 13. Twisted graphene hybrid structure. (a) The schematic picture of the hybrid transistor with BTG. (b), (c) The electric field distribution of the hybrid mode from side view for monolayer and bilayer twisted graphene structures, respectively.

expect to achieve a significant PL for the hybrid mode by utilizing the TBG in magic angles. However it should be noted that the hybrid mode has a plasmonic-photonic dual nature. This means that this mode is under the influence of both the plasmonic material (TBG) and the environment, especially the nanowire, which it takes us a little away from the ideal result.

Using the data reported in [74] and according to numeric calculations from the references [76,77], for the first magic angle of $\theta = 1.16^{\circ}$, $T = 70$ mK, and $B = 0$ T, the obtained hybrid mode has a strong confinement ($A/A_0 \sim 10^{-8}$) and ultralong propagation length in the order of meter, which is a wonderful result. The 3D simulation of the structure using the obtained data has been done in the beam envelope module of COMSOL. Figures 13(b) and 13(c) do a qualitative comparison between the PLs of the structures of monolayer graphene and TBG. Figures 13(b) and 13(c) display the picture of the hybrid mode from the structure side view in which the laser illumination has been done from the left side. It should be noted that, because of considerable difference of PL in two structures, the length of structures has been resized by the "camera" feature in COMSOL to provide a better representation. In the monolayer graphene structure [Fig. 13(b)], as the inset shows, the mode propagates only a few nanometers. By considering its high confinement, this hybrid mode could be presented as a hotspot. However, the hybrid mode in TBG structure has a considerable PL in addition to its very high confinement. An enlarged view of the end of the structure has been shown in the inset of Fig. 13(c), indicating that the propagation is still ongoing. The hybrid TBG structure is a great candidate for usage as an ultraconfined optical waveguide and in quantum computers.

VI. CONCLUSION

In summary, we have studied the hybrid plasmonic mode in a combined nanoelectronic structure including a graphene FET and a silicon nanowire by applying a laser light. The complicated two channel transport model has been used for graphene simulation, which results in interesting nonlinear behavior of the hybrid mode near the CNP. Furthermore, the obtained hybrid hotspot in this nanostructure presents high energy intensity, high degree of confinement, and tunable nanoscale PL, which can be proposed for nanoscale devices. Moreover, it could be a reference for high resolution atomic localization and precise optical tweezing.

ACKNOWLEDGMENTS

We would like to express our gratitude to Dr. M. Ranjbar and Dr. B. Ahmadi for their very great assistance.

[1] B. E. Saleh, M. C. Teich, and O. Fundamentals, *Photonics* (Wiley, New York, 2019).
[2] S. Bea and M. Teich, *Fundamentals of Photonics* (Wiley-Hnterscience, New York, 1991), p. 313.
[3] F. G. Smith, T. A. King, and D. Wilkins, *Optics and Photonics: An Introduction* (John Wiley & Sons, New York, 2007).
[4] N. I. Zheludev, Nat. Mater. **7**, 420 (2008).
[5] W. L. Barnes, A. Dereux, and T. W. Ebbesen, Nature (London) **424**, 824 (2003).
[6] S. A. Maier, *Plasmonics: Fundamentals and Applications* (Springer Science & Business Media, New York, 2007).

[7] J. A. Schuller, E. S. Barnard, W. Cai, Y. C. Jun, J. S. White, and M. L. Brongersma, Nat. Mater. **9**, 193 (2010).
[8] M. L. Brongersma and V. M. Shalaev, Science **328**, 440 (2010).
[9] M. Kauranen and A. V. Zayats, Nat. Photon. **6**, 737 (2012).
[10] W. Cai, A. P. Vasudev, and M. L. Brongersma, Science **333**, 1720 (2011).
[11] H. R. Seren, J. Zhang, G. R. Keiser, S. J. Maddox, X. Zhao, K. Fan, S. R. Bank, X. Zhang, and R. D. Averitt, Light Sci. Appl. **5**, e16078 (2016).
[12] M. Klein, B. H. Badada, R. Binder, A. Alfrey, M. McKie, M. R. Koehler, D. G. Mandrus, T. Taniguchi, K. Watanabe, B. J. LeRoy *et al.*, Nat. Commun. **10**, 3264 (2019).
[13] J. Lee, M. Tymchenko, C. Argyropoulos, P.-Y. Chen, F. Lu, F. Demmerle, G. Boehm, M.-C. Amann, A. Alu, and M. A. Belkin, Nature (London) **511**, 65 (2014).
[14] J. Anker, W. Hall, O. Lyandres, N. Shah, J. Zhao, and R. V. Duyne, Nat. Mater. **7**, 442 (2008).
[15] A. E. Cetin, A. F. Coskun, B. C. Galarreta, M. Huang, D. Herman, A. Ozcan, and H. Altug, Light Sci. Appl. **3**, e122 (2014).
[16] F. Yesilkoy, R. A. Terborg, J. Pello, A. A. Belushkin, Y. Jahani, V. Pruneri, and H. Altug, Light Sci. Appl. **7**, 17152 (2018).
[17] S. Kawata, Y. Inouye, and P. Verma, Nat. Photon. **3**, 388 (2009).
[18] J. Chen, M. Badioli, P. Alonso-González, S. Thongrattanasiri, F. Huth, J. Osmond, M. Spasenović, A. Centeno, A. Pesquera, P. Godignon *et al.*, Nature (London) **487**, 77 (2012).
[19] T. Xu, Y.-K. Wu, X. Luo, and L. J. Guo, Nat. Commun. **1**, 59 (2010).
[20] Y. J. Jang, K. Chung, J. S. Lee, C. H. Choi, J. W. Lim, and D. H. Kim, ACS Photon. **5**, 4711 (2018).
[21] V. V. Temnov, Nat. Photon. **6**, 728 (2012).
[22] X. Chen, B. Jia, Y. Zhang, and M. Gu, Light Sci. Appl. **2**, e92 (2013).
[23] E. Ozbay, Science **311**, 189 (2006).
[24] H. J. Lezec, A. Degiron, E. Devaux, R. Linke, L. Martin-Moreno, F. Garcia-Vidal, and T. Ebbesen, Science **297**, 820 (2002).
[25] R. Zia, J. A. Schuller, A. Chandran, and M. L. Brongersma, Mater. Today **9**, 20 (2006).
[26] A. Tuniz, O. Bickerton, F. J. Diaz, T. Käsebier, E.-B. Kley, S. Kroker, S. Palomba, and C. M. de Sterke, Nat. Commun. **11**, 2413 (2020).
[27] Y. Fang and M. Sun, Light Sci. Appl. **4**, e294 (2015).
[28] W. Du, T. Wang, H.-S. Chu, and C. A. Nijhuis, Nat. Photon. **11**, 623 (2017).
[29] U. Koch, C. Uhl, H. Hettrich, Y. Fedoryshyn, C. Hoessbacher, W. Heni, B. Baeuerle, B. I. Bitachon, A. Josten, M. Ayata *et al.*, Nat. Electron. **3**, 338 (2020).
[30] Z. Fei, A. Rodin, W. Gannett, S. Dai, W. Regan, M. Wagner, M. Liu, A. McLeod, G. Dominguez, M. Thiemens *et al.*, Nat. Nanotechnol. **8**, 821 (2013).
[31] A. Boltasseva and H. A. Atwater, Science **331**, 290 (2011).
[32] A. Hosseini and Y. Massoud, Opt. Express **14**, 11318 (2006).
[33] S. Xiao and N. A. Mortensen, *Optoelectronic Materials and Devices III* (International Society for Optics and Photonics, Bellingham, WA, 2008), Vol. 7135, p. 71352J.
[34] R. F. Oulton, V. J. Sorger, D. Genov, D. Pile, and X. Zhang, Nat. Photon. **2**, 496 (2008).
[35] K. S. Novoselov and A. Geim, Nat. Mater. **6**, 720 (2007).
[36] A. K. Geim, Science **324**, 1530 (2009).
[37] S. Stankovich, D. A. Dikin, G. H. Dommett, K. M. Kohlhaas, E. J. Zimney, E. A. Stach, R. D. Piner, S. T. Nguyen, and R. S. Ruoff, Nature (London) **442**, 282 (2006).
[38] K. S. Novoselov, A. K. Geim, S. V. Morozov, D. Jiang, Y. Zhang, S. V. Dubonos, I. V. Grigorieva, and A. A. Firsov, Science **306**, 666 (2004).
[39] A. H. Castro Neto, F. Guinea, N. M. R. Peres, K. S. Novoselov, and A. K. Geim, Rev. Mod. Phys. **81**, 109 (2009).
[40] O. C. Compton and S. T. Nguyen, Small **6**, 711 (2010).
[41] S. Patchkovskii, S. T. John, S. N. Yurchenko, L. Zhechkov, T. Heine, and G. Seifert, Proc. Natl. Acad. Sci. USA **102**, 10439 (2005).
[42] H. Lin, B. C. Sturmberg, K.-T. Lin, Y. Yang, X. Zheng, T. K. Chong, C. M. de Sterke, and B. Jia, Nat. Photon. **13**, 270 (2019).
[43] F. Bonaccorso, Z. Sun, T. Hasan, and A. Ferrari, Nat. Photon. **4**, 611 (2010).
[44] M. Ranjbar, R. Sbiaa, S. Mohseni, M. Rahimabady, and S. Piramanayagam, Mater. Today **19**, 368 (2016).
[45] G. Song, M. Ranjbar, D. R. Daughton, and R. A. Kiehl, Nano Lett. **19**, 7112 (2019).
[46] K. S. Novoselov, A. K. Geim, S. V. Morozov, D. Jiang, M. I. Katsnelson, I. Grigorieva, S. Dubonos, and A. A. Firsov, Nature (London) **438**, 197 (2005).
[47] Y. Zhang, Y.-W. Tan, H. L. Stormer, and P. Kim, Nature (London) **438**, 201 (2005).
[48] A. K. Geim and K. S. Novoselov, *Nanoscience and Technology: A Collection of Reviews from Nature Journals* (World Scientific, Singapore, 2010), pp. 11–19.
[49] F. Wang, Y. Zhang, C. Tian, C. Girit, A. Zettl, M. Crommie, and Y. R. Shen, Science **320**, 206 (2008).
[50] Y. Zhang, T.-T. Tang, C. Girit, Z. Hao, M. C. Martin, A. Zettl, M. F. Crommie, Y. R. Shen, and F. Wang, Nature (London) **459**, 820 (2009).
[51] J. Guo, J. Li, C. Liu, Y. Yin, W. Wang, Z. Ni, Z. Fu, H. Yu, Y. Xu, Y. Shi *et al.*, Light Sci. Appl. **9**, 29 (2020).
[52] R. Hao, Z. Ye, Y. Gu, X. Peng, H. Chen, and E. Li, Sci. Rep. **8**, 16830 (2018).
[53] S. Qu, C. Ma, and H. Liu, Sci. Rep. **7**, 5190 (2017).
[54] Y. Shen, S. Skirlo, N. C. Harris, D. Englund, and M. Soljačić, *CLEO: Science and Innovations* (Optical Society of America, Washington, DC, 2016), pp. SM3E–2.
[55] H. J. Caulfield, J. Kinser, and S. K. Rogers, Proc. IEEE **77**, 1573 (1989).
[56] S. Ishiwata, Y. Shiomi, J. Lee, M. Bahramy, T. Suzuki, M. Uchida, R. Arita, Y. Taguchi, and Y. Tokura, Nat. Mater. **12**, 512 (2013).
[57] K. Gopinadhan, Y. J. Shin, R. Jalil, T. Venkatesan, A. K. Geim, A. H. C. Neto, and H. Yang, Nat. Commun. **6**, 8337 (2015).
[58] C.-Z. Li, J.-G. Li, L.-X. Wang, L. Zhang, J.-M. Zhang, D. Yu, and Z.-M. Liao, ACS Nano **10**, 6020 (2016).
[59] A. Vakil and N. Engheta, Science **332**, 1291 (2011).
[60] A. Y. Nikitin, F. Guinea, F. J. Garcia-Vidal, and L. Martin-Moreno, Phys. Rev. B **84**, 195446 (2011).
[61] S. Adam, E. Hwang, V. Galitski, and S. D. Sarma, Proc. Natl. Acad. Sci. USA **104**, 18392 (2007).
[62] M. A. Yamoah, W. Yang, E. Pop, and D. Goldhaber-Gordon, ACS Nano **11**, 9914 (2017).

[63] G. Song, M. Ranjbar, and R. A. Kiehl, Commun. Phys. **2**, 65 (2019).
[64] S. Das Sarma, S. Adam, E. H. Hwang, and E. Rossi, Rev. Mod. Phys. **83**, 407 (2011).
[65] F. Rana, Phys. Rev. B **76**, 155431 (2007).
[66] Y. Sui and J. Appenzeller, Nano Lett. **9**, 2973 (2009).
[67] X. Luo, T. Qiu, W. Lu, and Z. Ni, Mater. Sci. Eng., R: Rep. **74**, 351 (2013).
[68] M. P. Nielsen, X. Shi, P. Dichtl, S. A. Maier, and R. F. Oulton, Science **358**, 1179 (2017).
[69] L. Zhang, D. Shi, T. J. Huang, R. Huang, and H. Gong, Nanoscale **9**, 18430 (2017).
[70] E. N. Bulgakov and D. N. Maksimov, Phys. Rev. A **96**, 063833 (2017).
[71] C. A. Valagiannopoulos and P. Alitalo, Phys. Rev. B **85**, 115402 (2012).
[72] C. A. Valagiannopoulos and N. K. Uzunoglu, IEEE Trans. Microwave Theory Tech. **55**, 1673 (2007).
[73] B. Rejaei and A. Khavasi, J. Opt. **17**, 075002 (2015).
[74] Y. Cao, V. Fatemi, S. Fang, K. Watanabe, T. Taniguchi, E. Kaxiras, and P. Jarillo-Herrero, Nature (London) **556**, 43 (2018).
[75] S. Carr, D. Massatt, S. Fang, P. Cazeaux, M. Luskin, and E. Kaxiras, Phys. Rev. B **95**, 075420 (2017).
[76] T. Stauber, P. San-Jose, and L. Brey, New J. Phys. **15**, 113050 (2013).
[77] A. V. Rozhkov, A. Sboychakov, A. Rakhmanov, and F. Nori, Phys. Rep. **648**, 1 (2016).